Highly Efficient Bridgeless Dual-Mode Resonant Single Power-Conversion AC–DC Converter

Sooa Kim, *Student Member, IEEE*, Bong-Hwan Kwon, *Member, IEEE*, and Minsung Kim, *Member, IEEE*

***Abstract*—This paper presents a bridgeless dual-mode single power-conversion ac–dc converter that can achieve a high conversion efficiency. By adopting a bidirectional switch, we remove a full-bridge diode rectifier from the grid side of the proposed converter, and thereby, reduce the number of components and the primary-side conduction loss. To adapt the converter to 1-kW power applications with a bidirectional switch, we used a series-resonant circuit in the output voltage doubler on the secondary side. The series-resonant circuit also provides zero-current switching turn-OFF at the output diode, and thereby, reduces the reverse-recovery loss. To attain medium–high power capability with an appropriate transformer, the proposed converter operates in both discontinuous conduction mode and continuous conduction mode. The operation principle of the converter is presented and analyzed. By using the dual-mode control algorithm, the proposed converter achieves a high power factor of 0.994 and maximum efficiency of 97.3%. Experimental results for a prototype 1-kW ac–dc converter verify these characteristics.**

***Index Terms*—AC–DC power conversion, bridgeless converter, bidirectional switch, continuous conduction mode (CCM), discontinuous conduction mode (DCM), series-resonant circuit.**

I. Introduction

POWER factor correction (PFC) ac–dc converters are widely used in grid-connected power-supply systems such as common dc bus suppliers in the buildings/mobile charging stations and electric-vehicle chargers. These PFC ac–dc converters must meet harmonic regulation requirements and standards such as IEC 61000-3-2 and IEEE 519; and at the same time should achieve high power density at low system cost. In addition, topologies should achieve a high conversion efficiency with low

Manuscript received March 23, 2018; revised June 28, 2018, September 7, 2018, and November 25, 2018; accepted January 17, 2019. Date of publication January 31, 2019; date of current version August 29, 2019. This work was supported in part by the Ministry of Science, ICT and Future Planning (MSIP), Korea, under the "ICT Consilience Creative Program" (IITP-R0346-16-1007) supervised by the Institute for Information and Communications Technology Promotion (IITP) and under Basic Science Research Program through the National Research Foundation of Korea (NRF) funded by the Ministry of Education (No. 2018R1D1A1B07044999). Recommended for publication by Associate Editor L. Huber. *(Corresponding author: Minsung Kim.)*

S. Kim is with the Department of Creative IT Engineering, Pohang University of Science and Technology (POSTECH), Pohang 37673, Korea (e-mail:

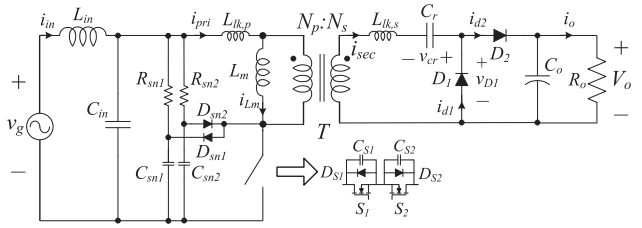

Fig. 1. Circuit diagram of the proposed converter with the bidirectional resistor–capacitor–diode (RCD) snubber. S_i, D_{Si}, and C_{Si} $(i = 1, 2)$: equivalent model parameters of the primary-side switches; R_{sni}, C_{sni}, and D_{sni} $(i = 1, 2)$: parameters of the bidirectional RCD snubber; D_1 and D_2: secondary diodes. T: transformer with turns ratio $n = N_s/N_p$, where N_p is the number of primary winding turns and N_s is the number of secondary winding turns. L_m: magnetizing inductance; $L_{\text{lk},p}$: primary leakage inductance; $L_{\text{lk},s}$: secondary leakage inductance; C_r: resonant capacitor; C_o: output capacitor; R_o: output load. v_g: grid voltage; $v_{C\,\text{in}}$: voltage across C_{in}; V_o: output voltage; v_{cr}: voltage across C_r; $v_{D\,1}$: voltage across D_1; i_{in}: input current; i_{pri}: primary-side current; $i_{L\,m}$: magnetizing current; i_{sec}: secondary-side current; i_{d1}: diode current through D_1; i_{d2}: diode current through D_2; and i_o: output current.

in cost, and low in conduction loss because it uses a single bidirectional switch instead of input bridge diodes. To obtain high power capability with a single bidirectional switch, the proposed converter uses a series-resonant circuit in the output voltage doubler on the secondary side. The series-resonant circuit achieves zero-current switching (ZCS) turn-OFF at the output diode and reduces the reverse-recovery loss. To achieve medium-high power capacity with appropriate size of the transformer, it operates in the discontinuous conduction mode (DCM) when the instantaneous power level is low and in the continuous conduction mode (CCM) when the instantaneous power level is high. Furthermore, the proposed converter can control the input current PF and can regulate the output voltage by using a dual-mode PFC control algorithm. The design guidelines of the proposed converter are presented and experimental results are obtained using a prototype 1-kW ac/dc converter.

This paper is organized as follows. The mode analysis of the proposed converter is described in Section II. A control algorithm used for the proposed converter is presented in Section III. The design guidelines of the proposed converter are described in Section IV. Experimental results and discussions are presented in Section V and the conclusions are drawn in Section VI.

II. Topology and System Description

Fig. 1 shows the circuit diagram of the proposed bridgeless single power-conversion ac–dc converter. The single bidirectional switch is used to transfer energy to the secondary side without rectifying the ac grid voltage. During the positive half cycle of the grid voltage v_g, the main switch S_1 is turned ON according to the duty ratio. During the negative half cycle of v_g, switch S_2 is turned ON and acts as the main switch. S_1 and S_2 operate complementary to each other. When the bidirectional switch is turned ON, the energy of the primary side is transferred to the secondary side through the series-resonant circuit [18], [19]. When the bidirectional switch is turned OFF, the energy charged in L_m is transferred to the secondary side. This characteristic enables the proposed converter to process high power

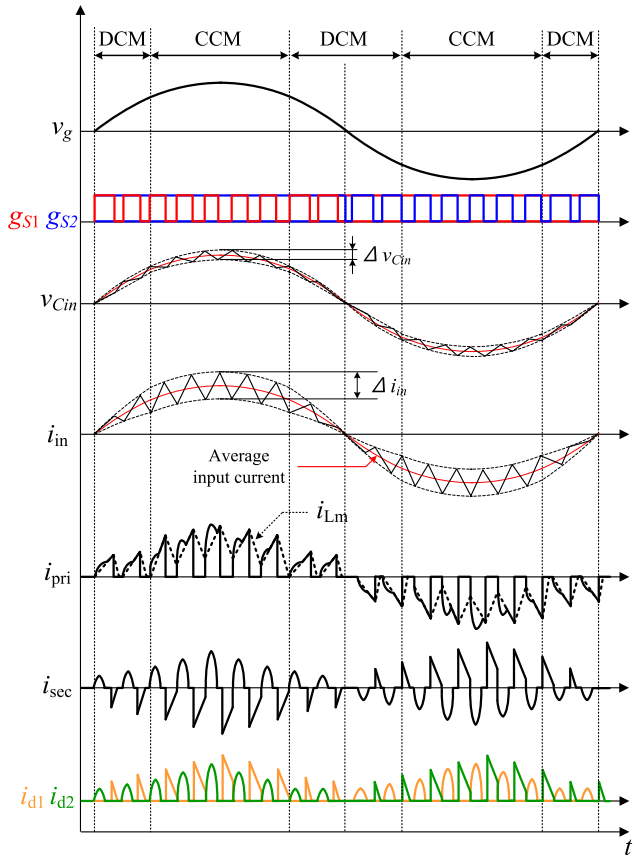

Fig. 2. DCM and CCM waveforms of the proposed converter during a grid period. $g_{S\,1}$ and $g_{S\,2}$ are the gate–source voltage of S_1 and S_2, respectively.

by using a bidirectional switch. The conventional RCD snubber cannot be used because it operates only when the grid voltage is positive. To reduce the voltage spike of the proposed converter in both positive and negative half cycles of the grid voltage, we use the bidirectional RCD snubber.

The proposed converter is designed to operate in the DCM at a low instantaneous power level, and in the CCM at a high instantaneous power level, so the waveform of the output current (see Fig. 2) represents this operation. The proposed converter requires less peak current and achieves higher efficiency when it operates in the CCM than when it operates in the DCM. As the magnetizing inductance L_m increases, the CCM region widens in a single grid period, and thereby, increases the power conversion efficiency. However, large L_m requires large transformer size, so L_m must be selected carefully to optimize the tradeoff between the efficiency and transformer size.

During the DCM steady-state operation, the switching period T_s is divided into five operating modes according to the switch and diode states. The equivalent circuit of each operating mode and the corresponding signal waveforms are shown in Figs. 3 and 4. During the CCM steady-state operation, T_s is divided into four operating modes according to the switch and diode states. The equivalent circuit of each operating modes and the signal waveforms are shown in Figs. 5 and 6. To analyze the steady-state operation of the proposed converter, we make several assumptions.

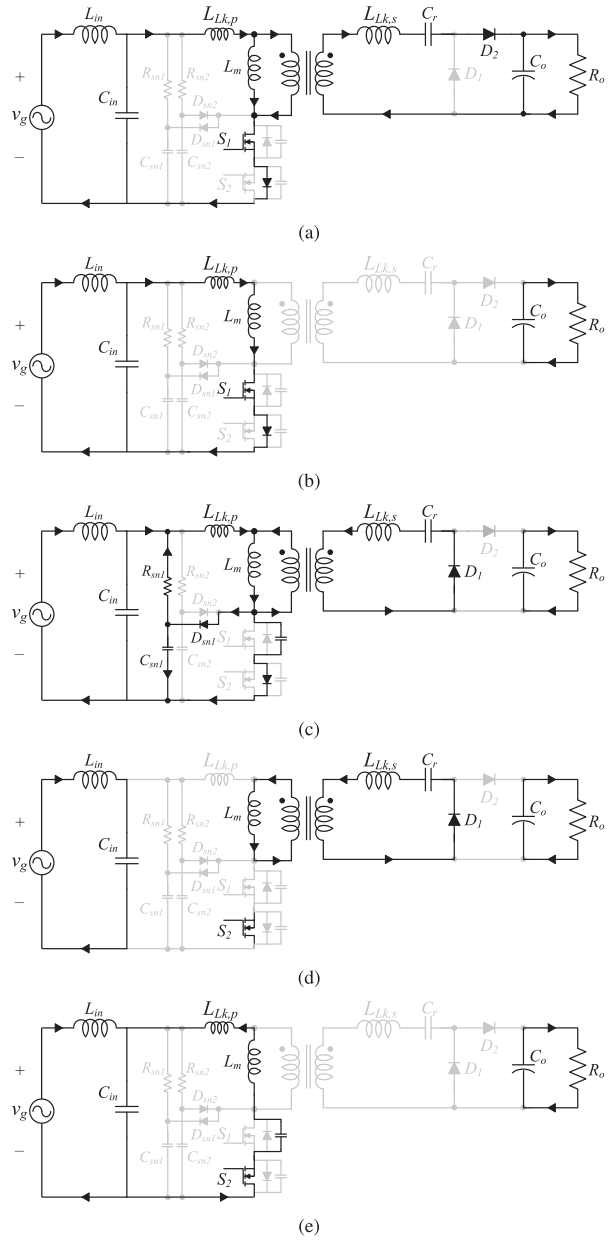

Fig. 3. Equivalent circuits during the switching period when the proposed converter operates in the DCM. (a) Mode 1. (b) Mode 2. (c) Mode 3. (d) Mode 4. (e) Mode 5.

1) The grid voltage v_g is constant because the switching frequency f_s is much higher than the grid frequency f_g.
2) The output capacitor C_o is sufficiently large that the output voltage V_o is assumed to have no ripple voltage.
3) The transformer T is ideal with the magnetizing inductance L_m, the primary leakage inductance $L_{\mathrm{lk},p}$, and the secondary leakage inductance $L_{\mathrm{lk},s}$.
4) The switch S_1 is modulated with duty ratio D, and the switch S_2 is complementary to S_1 with a short dead time.

A. DCM Operation

1) Mode 1 [t_0, t_1]: At time t_0, S_1 is turned ON. i_{sec} begins to resonate due to $L_{\mathrm{lk},s}$ and C_r and it is directly delivered to the load through D_2. For the simplicity, we ignored the input filter effect and considered $v_{C\mathrm{in}}$ as v_g; v_g is considered to be constant during T_s. Also, we assume that $L_m \gg L_{\mathrm{lk},p}$ for the brevity. Then, i_{Lm} increases linearly as

$$\frac{di_{Lm}(t)}{dt} = \frac{v_g}{L_m}. \tag{1}$$

During this interval, the input power is directly transferred to the output stage of the transformer and charges the magnetic inductor. Since $L_m \gg L_{\mathrm{lk},p}$, the secondary-side voltage of the transformer can be expressed as nv_g. And the state equation of the circuit can be written as

$$L_{\mathrm{lk},s}\frac{di_{\mathrm{sec}}(t)}{dt} = nv_g - V_o + v_{cr}(t) \tag{2}$$

$$i_{\mathrm{sec}}(t) = -C_r\frac{dv_{cr}(t)}{dt} \tag{3}$$

with $i_{\mathrm{sec}}(t_o) = 0$, where v_{cr} is the voltage across C_r. Solving (2) and (3) yields

$$i_{\mathrm{sec}}(t) = \frac{nv_g - (V_o - v_{cr}(t_0))}{Z_r}\sin\left[w_r(t-t_0)\right] \tag{4}$$

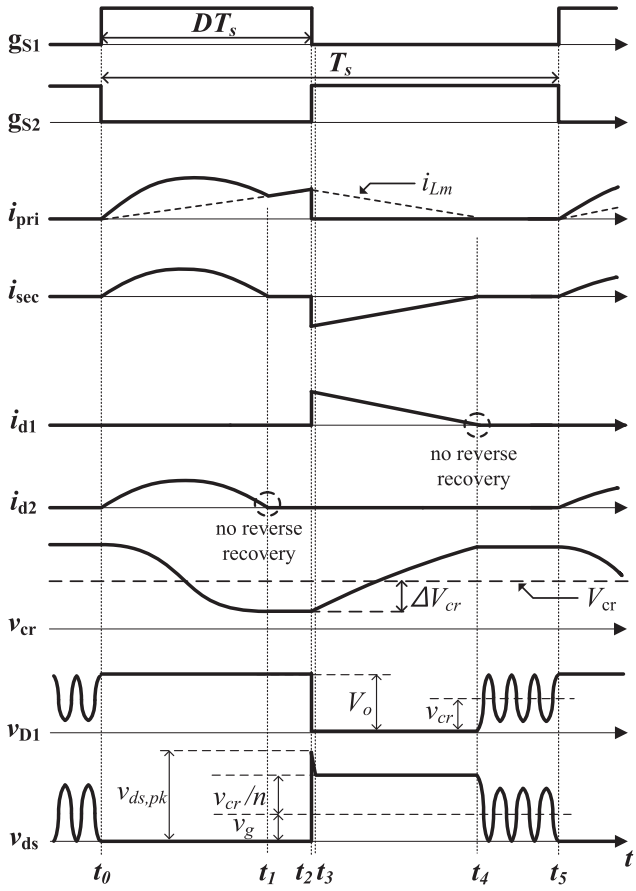

Fig. 4. Waveforms of the proposed converter during the DCM. v_{ds} is the drain–source voltage of S_1.

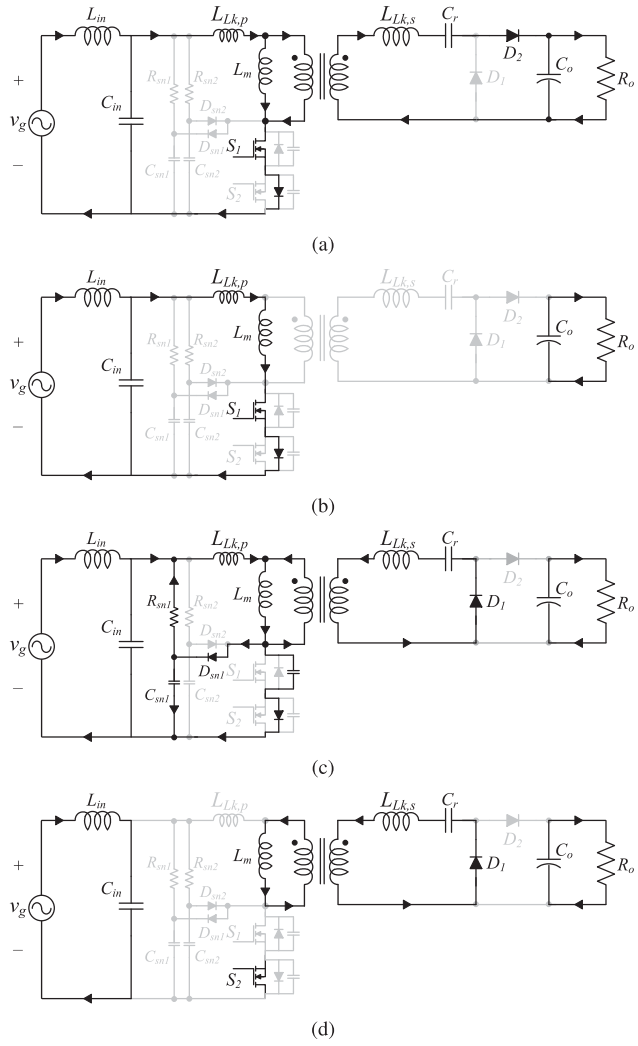

Fig. 5. Equivalent circuits during the switching period when the proposed converter operates in the CCM. (a) Mode 1. (b) Mode 2. (c) Mode 3. (d) Mode 4.

where the resonant angular frequency w_r and the characteristic impedance Z_r are given by

$$w_r = \frac{1}{\sqrt{L_{\mathrm{lk},s} C_r}}, Z_r = \sqrt{\frac{L_{\mathrm{lk},s}}{C_r}}. \tag{5}$$

At the same time, the input power charges L_m, and i_{Lm} is increased linearly as

$$i_{Lm}(t) = \frac{v_g}{L_m}(t - t_0). \tag{6}$$

2) Mode 2 [t_1, t_2]: At time t_1, the resonance between $L_{\mathrm{lk},s}$ and C_r terminates and i_{sec} becomes zero. D_2 is turned OFF with zero current, and therefore, does not have reverse-recovery loss. The input power still charges L_m, and i_{Lm} increases linearly as

$$i_{Lm}(t) = i_{Lm}(t_1) + \frac{v_g}{L_m}(t - t_1) = \frac{v_g}{L_m}(t - t_0). \tag{7}$$

3) Mode 3 [t_2, t_3]: At time t_2, S_1 is turned OFF and i_{Lm} is transferred to the secondary side. A high-voltage spike occurs at the switch because turned-OFF of the switch interrupts the current flowing through the leakage inductance of the transformer.

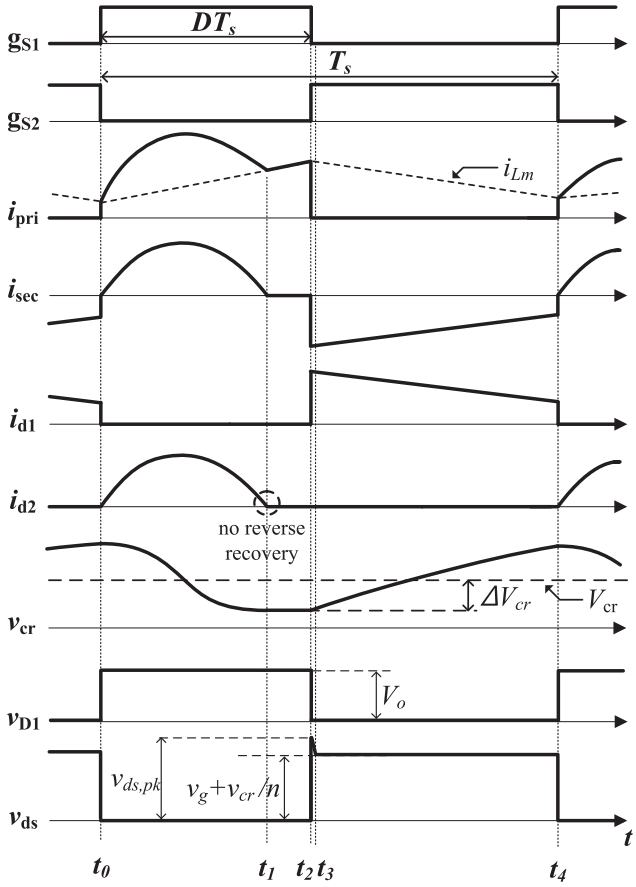

Fig. 6. Waveforms of the proposed converter in the CCM.

Here, the RCD snubber circuit absorbs the current in the primary leakage inductor by turning ON the snubber diode when v_{ds} exceeds $v_g + v_{cr}/n$.

4) Mode 4 [t_3, t_4]: i_{sec} already begins to resonate due to L_m and C_r at t_2. $i_{Lm}(t_2)$ is reflected on the initial value of the secondary-side current $i_{\mathrm{sec}}(t_2)$, which becomes $i_{\mathrm{sec}}(t_2) = -i_{Lm}(t_2)/n$. Then, the state equation of i_{sec} can be written as

$$n^2 L_m \frac{di_{\mathrm{sec}}(t)}{dt} = v_{cr}(t) \tag{8}$$

$$i_{\mathrm{sec}}(t) = -C_r \frac{dv_{cr}(t)}{dt} \tag{9}$$

with $i_{\mathrm{sec}}(t_2) = -v_g DT/nL_m$ and $v_{cr}(t_2) = V_{cr} - \Delta V_{cr}$. Solving (8) and (9) yields

$$i_{\mathrm{sec}}(t) = -\frac{v_g DT_s}{nL_m} \cos w_{cr}(t - t_2) + \frac{V_{cr} - \Delta V_{cr}}{n^2 L_m w_{cr}} \sin w_{cr}(t - t_2) \tag{10}$$

where $w_{cr} = 1/\sqrt{n^2 L_m C_r}$ and V_{cr} is the average voltage of the resonant capacitor C_r. Since $w_{cr}(t - t_2)$ is very small, $\cos w_{cr}(t - t_2) \simeq 1$ and $\sin w_{cr}(t - t_2) \simeq w_{cr}(t - t_2)$. Also, $V_{cr} \gg \Delta V_{cr}$ with appropriate value of C_r. For the simplicity,

we consider $V_{cr} - \Delta V_{cr}$ as V_{cr} in this interval. Then, we have

$$i_{\text{sec}}(t) \simeq -\frac{v_g}{nL_m} DT_s + \frac{V_{cr}}{n^2 L_m}(t - t_2). \tag{11}$$

5) Mode 5 [t_4, t_5]: At time t_4, i_{sec} becomes zero. D_1 is turned OFF with zero current, and therefore, does not have reverse-recovery loss. t_4 can be calculated from (11) as

$$t_4 = t_2 + \frac{nv_g DT_s}{V_{cr}}. \tag{12}$$

Since the secondary current becomes zero, the diode D_1 is turned OFF. The residual energy in the circuit causes the resonance between C_{S1}, L_m, and $L_{\text{lk},p}$, which generates the sinusoidal oscillation of v_{ds} in the interval t_3 and t_4. Meanwhile, this oscillation is reflected to v_{D1} (see Fig. 4).

During the negative grid voltage period, the circuit waveforms are similar to those of Modes 1–5.

B. CCM Operation

1) Mode 1 [t_0, t_1]: At time t_0, S_1 is turned ON and i_s begins to flow through D_2. v_g is approximately constant during T_s, so i_{sec} becomes

$$i_{\text{sec}}(t) = \frac{nv_g - (V_o - v_{cr}(t_0))}{Z_r} \sin\left[w_r(t - t_0)\right]. \tag{13}$$

At the same time, the input power charges L_m and i_{Lm} increases linearly as

$$i_{Lm}(t) = i_{Lm}(t_0) + \frac{v_g}{L_m}(t - t_0) \tag{14}$$

where $i_{Lm}(t_0)$ is the initial value of $i_{Lm}(t)$.

2) Mode 2 [t_1, t_2]: At time t_1, the resonance between $L_{\text{lk},s}$ and C_r terminates and i_{sec} becomes zero. D_2 is turned OFF with zero current, and therefore, does not have reverse-recovery loss. The input power charges the magnetic inductor and i_{Lm} increases linearly as

$$\begin{aligned} i_{Lm}(t) &= i_{Lm}(t_1) + \int_{t_0}^{t} \frac{v_{C\text{in}}(t)}{L_m} dt \\ &\simeq i_{Lm}(t_0) + \frac{v_g}{L_m}(t - t_0). \end{aligned} \tag{15}$$

3) Mode 3 [t_2, t_3]: At time t_2, S_1 is turned OFF and i_{Lm} is transferred to the secondary side. Similar to the DCM operation, the RCD snubber circuit absorbs the primary leakage current.

4) Mode 4 [t_3, t_4]: Similar to i_{sec} in DCM, i_{sec} in CCM can be obtained as

$$i_{\text{sec}}(t) \simeq -\frac{v_g}{nL_m} DT_s + \frac{V_{cr}}{n^2 L_m}(t - t_2). \tag{16}$$

During the CCM operation, i_{sec} never goes to zero. $i_{Lm}(t_4) = i_{Lm}(t_0)$ and $i_{Lm}(t_0)$ can then be described as

$$i_{Lm}(t_0) = i_{Lm}(t_2) + \frac{V_{cr}}{nL_m}(1 - D)T_s. \tag{17}$$

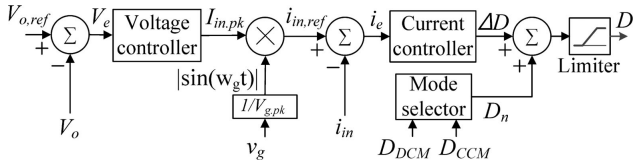

Fig. 7. Proposed control block diagram. $V_{o,\text{ref}}$ is the reference voltage output; V_e is the output voltage error; $I_{\text{in.pk}}$ is the peak value of the input current; $V_{g\text{.pk}}$ is the peak value of the grid voltage; $i_{\text{in,ref}}$ is the reference input current; i_e is the input current error; ΔD is the controller duty ratio; and D_n is the nominal duty ratio.

III. Controller Design

A. Controller Structure

To regulate the output voltage and achieve high PF, the proposed bridgeless converter uses control algorithms (see Fig. 7) in the outer loop output voltage regulation part and in the inner loop current control part. The inner and outer control loops are used to achieve high PF and to control output voltage.

The voltage controller part determines the output voltage error first by subtracting V_o from $V_{o\text{.ref}}$. This error is then supplied as an input to the proportional-integral controller. The controller output $I_{\text{in.pk}}$ is then used to generate the amplitude of the input current reference $i_{\text{in,ref}}$ as shown in Fig. 7. To achieve a high PF, the phase of the average input current must be synchronized with that of the average input voltage $v_g = \sqrt{2}V_{g\text{.rms}} \sin(w_g t)$ where $V_{g\text{.rms}}$ is the root-mean-squared (RMS) amplitude and w_g is angular frequency. $i_{\text{in,ref}}$ can then be determined as

$$i_{\text{in,ref}} = \sqrt{2} I_{\text{in.rms}} \sin(w_g t) = I_{\text{in.rms}} \cdot \frac{v_g}{V_{g\text{.rms}}} \tag{18}$$

where $I_{\text{in.rms}}$ is the RMS amplitude of $i_{\text{in,ref}}$.

Next, the current controller part obtains the input current error by subtracting i_{in} from $i_{\text{in.ref}}$. This error is then supplied as an input to the proportional-repetitive controller [20]–[22]. The controller output ΔD is then added with D_n to produce D, which is used to control the bidirectional switch, which in turn, drives the input current to track the reference one. To reduce the burden from the current controller, we use D_n as a feed-forward control input.

B. Calculation of Nominal Duty Ratio

Assuming that the converter is ideal with no power loss and that the input current tracks the reference one perfectly, we can describe the power balance equation as

$$V_{g\text{.rms}} I_{\text{in.rms}} = V_o I_o = P_o \tag{19}$$

$$v_g i_{\text{in.ref}} = V_o I_{d2} = 2P_o \sin^2(w_g t) \tag{20}$$

where I_o and I_{d2} are, respectively, the average output current and the average diode current over a switching period, and P_o is the output power.

In the DCM, the energy stored in C_r is discharged through D_1 and transferred to the load. The energy discharged from C_r is recovered by the energy stored in L_m. Applying the charge balance condition to C_r implies that the area of i_{sec} in mode 1 must be the same as the area of i_{sec} in mode 3. I_{d2} can then be

calculated as

$$I_{d2} = \frac{1}{T_s}\int_{t_0}^{t_1} i_{\text{sec}}(\tau)d\tau = \frac{i_{\text{sec}}(t_2)}{2T_s}(t_3 - t_2). \tag{21}$$

Substituting (10), (12), and (20) into (21), yields

$$\frac{2P_o}{V_o}\sin^2(w_g t) = \frac{v_g^2 D^2 T_s}{2L_m V_{cr}}. \tag{22}$$

On the other hand, applying the volt–second balance law for T yields

$$\frac{n^2 L_m}{n^2 L_m + L_{\text{lk},s}}(V_{cr} - V_o) = -nv_g \tag{23}$$

and because $L_m \gg L_{\text{lk},s}$, (23) can be approximated as

$$V_{cr} = V_o - nv_g. \tag{24}$$

Substituting (24) into (22) yields

$$\frac{2P_o}{V_o}\sin^2(w_g t) = \frac{v_g^2 D^2 T_s}{2L_m(V_o - nv_g)} \tag{25}$$

from which we can determine the nominal duty ratio D_{DCM} as

$$D_{\text{DCM}} = \sqrt{\frac{2L_m P_o}{T_s V_o V_{g.\text{rms}}^2}(V_o - nv_g)}. \tag{26}$$

During the CCM, applying the volt–second balance condition to L_m, it follows that

$$V_{cr} = \frac{nD}{1-D}v_g. \tag{27}$$

By substituting (24) into (27), we can represent the nominal duty ratio D_{CCM} as

$$D_{\text{CCM}} = 1 - \frac{nv_g}{V_o} = 1 - \frac{\sqrt{2}nV_{g,\text{rms}}\sin(w_g t)}{V_o}. \tag{28}$$

The resulting nominal duty D_n for the proposed dual-mode converter is obtained as

$$D_n = \begin{cases} D_{\text{DCM}}, & \text{if} \quad D_{\text{DCM}} < D_{\text{CCM}} \\ D_{\text{CCM}}, & \text{if} \quad D_{\text{DCM}} \geq D_{\text{CCM}}. \end{cases} \tag{29}$$

The converter operates in the DCM if $D_{\text{DCM}} \leq D_{\text{CCM}}$, and in the CCM otherwise. Although D_n does not directly determine the output current, the use of D_n helps the proposed converter generate the desired output voltage while reducing the burden from the feedback controller. Fig. 8 shows the nominal duty in the DCM and CCM at full load.

By equating D_{DCM} with D_{CCM}, we can determine the critical grid voltage $v_{g.\text{crit}}$ and the critical duty-ratio D_{crit}. Substituting (26) and (28) into $D_{\text{DCM}} = D_{\text{CCM}}$ yields

$$\sqrt{\frac{2L_m P_o}{T_s V_o V_{g.\text{rms}}^2}(V_o - nv_g)} = 1 - \frac{nv_g}{V_o}. \tag{30}$$

Squaring both sides of (30) and dividing both sides of it by $1 - \frac{nv_g}{V_o}$, yields

$$\frac{2L_m P_o}{T_s V_{g.\text{rms}}^2} = 1 - \frac{nv_g}{V_o}. \tag{31}$$

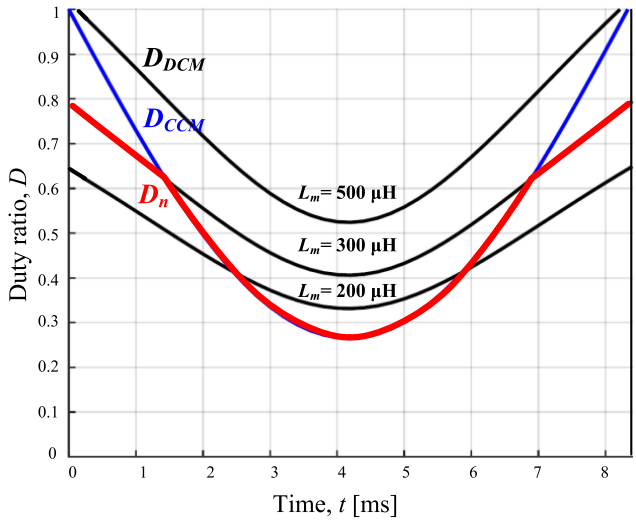

Fig. 8. Nominal duty ratio of the proposed converter at three inductances.

Then, we have the critical grid voltage

$$v_{g.\text{crit}} = \frac{V_o}{n} - \frac{2L_m P_o V_o}{nT_s V_{g.\text{rms}}^2}. \tag{32}$$

Then, substituting (31) into (28), we can determine the critical duty ratio

$$D_{\text{crit}} = \frac{2L_m P_o}{T_s V_{g.\text{rms}}^2}. \tag{33}$$

IV. Design Guidelines

A. Determining Resonant Capacitance

To guarantee ZCS turn-OFF at the output diode D_2, half of the resonant period must be smaller than the minimum turn-ON time of the switch or

$$\pi\sqrt{L_{\text{lk},s}C_r} < D_{\text{min}}T_s. \tag{34}$$

From Fig. 8, the minimum duty ratio D_{min} can be approximated as

$$D_{\text{min}} = 1 - \frac{\sqrt{2}nV_{g,\text{rms}}}{V_o} \tag{35}$$

from which

$$C_r < \frac{T_s^2}{\pi^2 L_{\text{lk},s}}\left(1 - \frac{\sqrt{2}nV_{g,\text{rms}}}{V_o}\right)^2 \tag{36}$$

follows.

B. Determining Magnetizing Inductance

Using the parameters given in Table I , we can depict the DCM and CCM regions as in Fig. 9 during half of the grid period. The proposed converter operates in the DCM when $v_g \leq v_{g,\text{crit}}$, and in the CCM otherwise. The boundary between the DCM and CCM is determined by L_m. Increase in L_m widens the CCM region, and increases the power conversion efficiency, but it increases the cost and size of the converter. Thus, L_m must be chosen appropriately.

TABLE I
PARAMETERS AND COMPONENTS OF THE PROTOTYPE

Parameters	Symbols	Value
Grid voltage	v_g	120–240 V
Grid frequency	f_g	60 Hz
Output voltage	V_o	360 V
Rated output power	P_o	1 kW
Switching frequency	f_s	50 kHz
Primary inductor	L_{in}	940 μH
Primary capacitor	C_{in}	6.6 μF
Magnetizing inductance	L_m	300 μH
Primary leakage inductance	$L_{lk,p}$	1.39 μH
Secondary leakage inductance	$L_{lk,s}$	0.86 μH
Snubber resistance	R_{sn1}, R_{sn2}	200 kΩ
Snubber capacitance	C_{sn1}, C_{sn2}	22 nF
Transformer turns ratio	N_p:N_s	28:22
Resonant capacitance	C_r	4.4 μF
Output capacitance	C_o	1320 μF
Components	**Symbol**	**Part number**
Primary-side switches	S_1, S_2	UJC06505K
Secondary-side diodes	D_1, D_2	F15U40S
Snubber diodes	D_{sn1}, D_{sn2}	UF4007
Transformer core	T	PQ5050

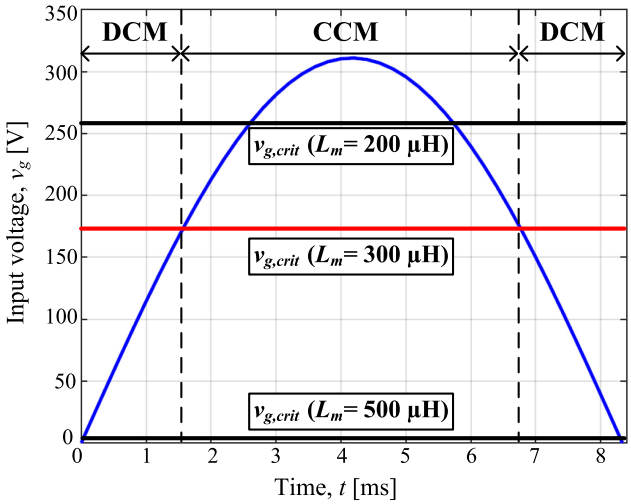

Fig. 9. DCM and CCM region according to different L_m values.

C. Determining Output Capacitance

To satisfy the output voltage ripple, we should select the output capacitor as

$$C_o \geq \frac{P_o}{2\pi f_g V_o \Delta V_o} \tag{37}$$

where ΔV_o is the output voltage ripple.

D. Selecting Transformer Turns Ratio

The turns ratio of the transformer can be selected from the voltage gain of the proposed converter. Rearranging (26) or (28), we have

$$n \leq \frac{V_o}{\sqrt{2} M_{\min} V_{g,\text{rms}}} = \frac{V_o}{\sqrt{2} V_{g,\text{rms}}} \tag{38}$$

where $M_{\min}$ is the minimum value of M, which is equal to 1.

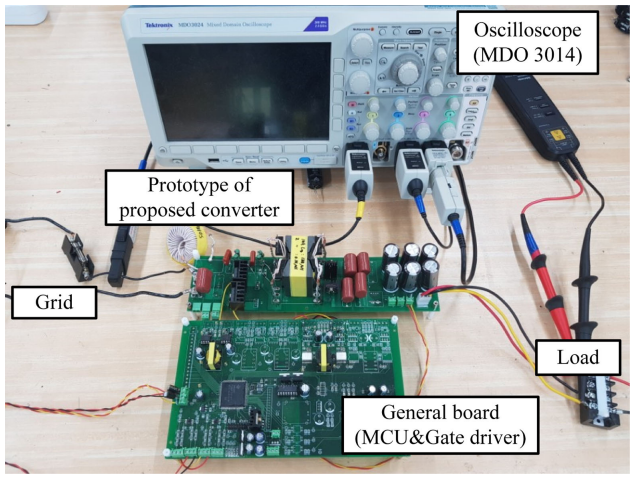

Fig. 10. Experimental setup of the proposed converter.

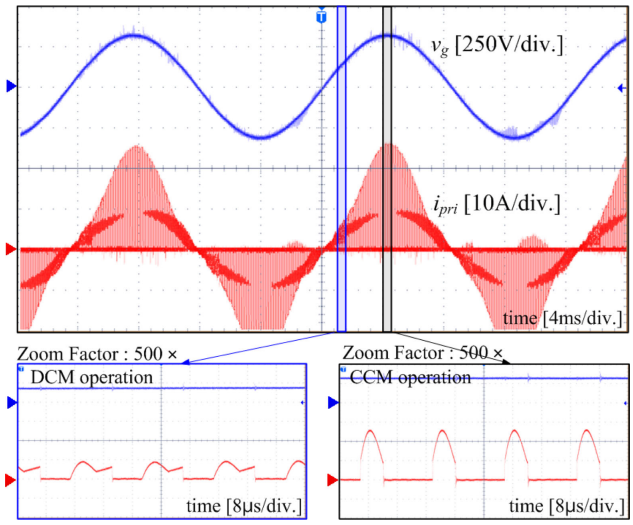

Fig. 11. Experimental waveforms of the grid voltage v_g and the primary-side current i_{pri}.

V. EXPERIMENTAL RESULTS AND DISCUSSIONS

To evaluate the efficiency of the proposed converter, we conducted experimental tests using a 1-kW prototype converter (see Fig. 10) with the grid voltage v_g = 120–240 V_{rms}; output voltage V_o = 360 V; and rated output power P_o = 1 kW. To satisfy ZCS turn-OFF at D_2 over the entire grid period, C_r is set to 4.4 μF. Considering the cost and size of the converter, L_m was set to 300 μH. Using (38), the turns ratio of the transformer is selected as $n = 0.79$. The general circuit parameters and the selected specific components (see Table I) were the same as in the analysis. We used a TMS320F28377D digital signal processor to implement the controller for the proposed converter.

The grid voltage and the primary-side current were measured in the DCM and CCM (see Fig. 11). When the current waveforms were almost sinusoidal and the resonance operation ended before the primary switch was turned OFF, the current resonated fully with low hard-switching loss. When the primary switch was turned OFF before the resonance operation ended, a significant amount of the current was left, so hard-switching loss

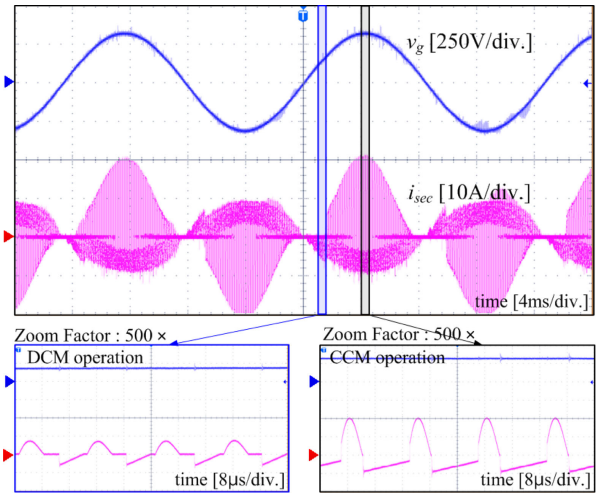

Fig. 12. Experimental waveforms of the grid voltage v_g and the secondary-side current $i_{\rm sec}$.

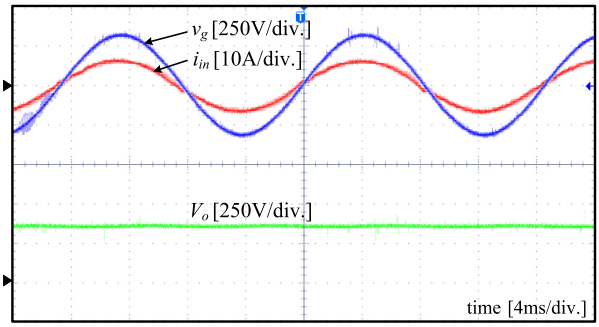

Fig. 13. Experimental waveforms of the grid voltage v_g, the input current $i_{\rm in}$, and the output voltage V_o at full load.

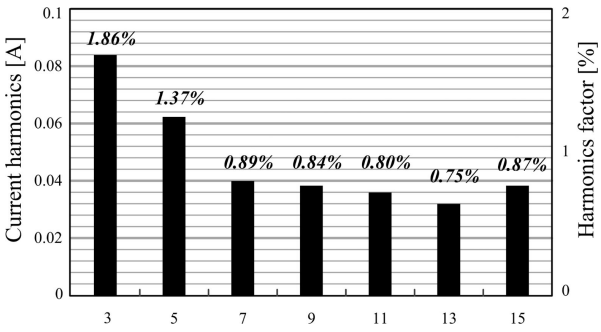

Fig. 14. Harmonics distribution of the measured input current.

was high. The grid voltage and the secondary-side current were measured in the DCM and CCM (see Fig. 12). During the ON switching period, the waveform of i_{d2} is the same as the waveform of $i_{\rm sec}$. During the OFF switching period, the waveform of i_{d1} is the same as the waveform of $-i_{\rm sec}$. The ZCS turn-OFFs at D_1 and D_2 were achieved in DCM. Thus, the switching loss is considerably reduced and reverse recovery loss is significantly reduced. During the CCM, ZCS turn-OFF is guaranteed only at D_2. The input current was almost sinusoidal and achieved the desired power level of 1 kW (see Fig. 13). The input current $i_{\rm in}$ was synchronized with v_g and had measured PF $= 0.994$.

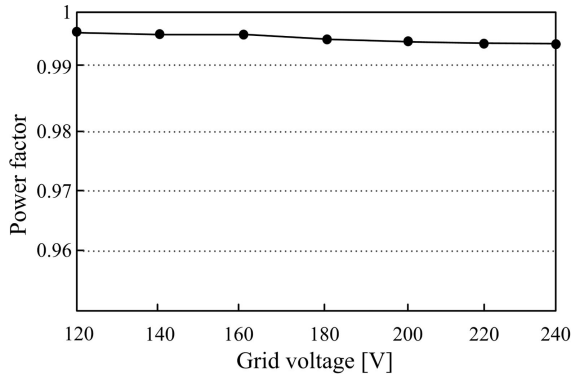

Fig. 15. Measured PF under entire grid voltage range.

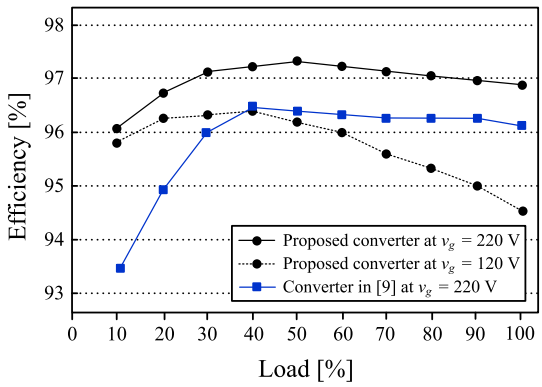

Fig. 16. Efficiency comparison of the proposed converter and converter in [9] when $v_g = 220$ V and $v_g = 120$ V.

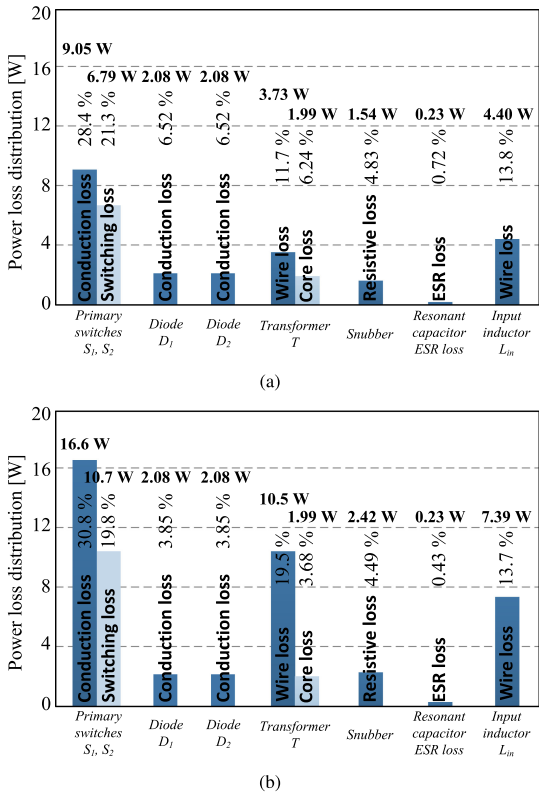

Fig. 17. Power loss distribution of the proposed converter at full load. (a) When $v_g = 220$ V. (b) When $v_g = 120$ V.

TABLE II
COMPARISON OF THE CONVENTIONAL BRIDGELESS CONVERTERS VERSUS THE PROPOSED CONVERTER

Items		[12]	[13]	[17]	Proposed converter
Topology		Bridgeless half-bridge converter	Bridgeless boost flyback converter	Bridgeless flyback converter	Bridgeless dual-mode resonant converter
Operation modes		CCM	DCM	DCM	DCM+CCM
Current waveforms		Linear	Linear	Linear	Resonant + Linear
Number of components	Switches	2	2	2	2
	Diodes	4	4	2	2
	Inductors	2	2	0	0
	Capacitors	3	3	1	2
Transformer type		Center-tapped	Normal	Center-tapped	Normal
Maximum efficiency		93%	92%	90%	97.3%
Efficiency at full load		93%	91.8%	88.3%	96.8%
Input voltage		90 V	90–240 V	90–140 V	120–240 V
Output voltage		48 V	48 V	48 V	360 V
Rated power		250 W	60 W	72 W	1 kW
Cost		High	High	Medium	Low
Circuit design		Medium	Medium	Medium	Simple

The PF and power conversion efficiency were measured by the Yokogawa WT3000E digital power meter. All harmonic components are in compliance with the IEC 61000-3-2 Class A standard and the measured total harmonic distortion $\leq$ 3.4 % under full-load and ac grid voltage 220 V (see Fig. 14). Measured PF was $\geq$ 0.994 over the entire grid voltage range (see Fig. 15). The maximum power conversion efficiency was 97.3% and the California Energy Commission (CEC) weighted efficiency was 97.1% at the ac grid voltage 220 V (see Fig. 16). The full-load efficiencies are 96.8% and 94.5% when the ac grid voltages are 220 and 120 V, respectively. The efficiency of the converter in [9] is 2% less than that of the proposed converter at the full load. Fig. 17 shows the power loss distribution of the proposed converter at full-load when v_g are 220 and 120 V. In Fig. 17(a), the primary switch loss takes 49.7% and the secondary diode loss takes 13.04% in total power loss when $v_g = 220$ V. In Fig. 17(b), the primary switch loss takes 50.6% and the secondary diode loss takes 7.7% in total power loss when $v_g = 120$ V.

We compare the number of components, operation modes, current waveforms, and power conversion efficiency of our proposed converter and other bridgeless converters (see Table II). For fair comparison, the input filter was not included when the number of power components was counted. Two bridgeless converters [12] and [13] suffer from large number of components; another [17] requires fewer components than [12] and [13] but has a flyback structure that limits its rated output power, because the center-tapped transformer requires a large core due to poor transformer utilization. The proposed converter uses a series-resonant voltage-doubler and single winding transformer, these components enable compact circuit design. The dual-mode operation reduces the size of the transformer even further while achieving a high power conversion efficiency. Moreover, thanks to series resonance operation, the proposed converter can achieve high efficiency and low switching stress of the proposed circuit.

Remark 1: The conventional forward converter recycles the magnetizing energy in the transformer to the input source by adding additional reset winding. On the other hand, the proposed converter operates similar to the forward converter and transfers the energy to the load in resonant way during the half switching period. Then, the proposed converter transfers the magnetizing energy in the transformer to the series-resonant circuit during other half switching period. Thanks to the inherent resonant voltage doubler structure on the secondary side, it does not require additional winding to reset the transformer.

Remark 2: The proposed converter is an isolated boost-type ac/dc converter. The primary application of the converter is common dc-bus supplier in the buildings/mobile charging stations [23]. Also, it can be used as a level-2 battery charger by connecting the proposed converters in parallel [24]. Furthermore, it can be used in high voltage applications such as medical X-ray imaging, traveling wave tube, and lasers [25].

VI. CONCLUSION

This paper presents a bridgeless dual-mode single power-conversion ac–dc converter. To reduce the number of components, the grid-side full-bridge diode rectifier was replaced by a bidirectional single switch; as a result, the number of components and the primary-side conduction loss were both reduced. Use of a series-resonant voltage-doubler structure reduced the size and cost of the implemented converter and enabled its use in medium-high power applications. To achieve medium-high power capacity with a given size of the transformer, the proposed converter uses dual-mode operation. Moreover, by using the dual-mode control, the proposed converter achieves high PF

and accurate output voltage regulation. We derive the mode analysis of the dual-mode operation and propose the design guideline of the proposed converter. To confirm the validity of the proposed converter, a 1-kW prototype converter was built and used for experimental tests. The proposed converter achieved maximum efficiency of 97.3% when $v_g = 220$ V at 50% load by means of the bridgeless power conversion structure and the turn-OFF ZCS mechanism of the output diode.

ACKNOWLEDGMENT

The authors would like to thank Dr. J. S. Lee for his assistance in this paper.

REFERENCES

[1] 80 Plus Incentive Program, 2019. [Online]. Available: http://www.80plus.org

[2] M. Narimani and G. Moschopoulos, "A new interleaved three-phase single-stage PFC AC-DC converter with flying capacitor," *IEEE Trans. Power Electron.*, vol. 30, no. 7, pp. 3695–3702, Jul. 2015.

[3] B. Poorali and E. Adib, "Analysis of the integrated SEPIC-flyback converter as a single-stage single-switch power-factor-correction LED driver," *IEEE Trans. Ind. Electron.*, vol. 63, no. 6, pp. 3562–3570, Jun. 2016.

[4] H. Ma, J. S. J. Lai, C. Zheng, and P. Sun, "A high-efficiency quasi-single-stage bridgeless electrolytic capacitor-free high-power AC-DC driver for supplying multiple LED strings in parallel," *IEEE Trans. Power Electron.*, vol. 31, no. 8, pp. 5825–5836, Aug. 2016.

[5] P. Fang and Y. F. Liu, "Energy channeling LED driver technology to achieve flicker-free operation With true single stage power factor correction," *IEEE Trans. Power Electron.*, vol. 32, no. 5, pp. 3892–3907, May 2017.

[6] S. Li, W. Qi, S. C. Tan, and S. R. Hui, "A single-stage two-switch PFC rectifier with wide output voltage range and automatic AC ripple power decoupling," *IEEE Trans. Power Electron.*, vol. 32, no. 9, pp. 6971–6982, Sep. 2017.

[7] Y. W. Cho, J. M. Kwon, and B. H. Kwon, "Single power-conversion AC–DC converter with high power factor and high efficiency," *IEEE Trans. Power Electron.*, vol. 29, no. 9, pp. 4797–4806, Sep. 2014.

[8] S. G. Jeong, W. J. Cha, S. H. Lee, J. M. Kwon, and B. H. Kwon, "Electrolytic capacitor-less single-power-conversion on-board charger with high efficiency," *IEEE Trans. Ind. Electron.*, vol. 63, no. 12, pp. 7488–7497, Dec. 2016.

[9] K. S. Kim, J. M. Kwon, and B. H. Kwon, "Single-switch single power-conversion PFC converter using regenerative snubber," *IEEE Trans. Ind. Electron.*, vol. 65, no. 7, pp. 5436–5444, Jul. 2018.

[10] L. Huber, Y. Jang, and M. M. Jovanovic, "Performance evaluation of bridgeless PFC boost rectifiers," *IEEE Trans. Power Electron.*, vol. 23, no. 3, pp. 1381–1390, Mar. 2008.

[11] B. Su, J. Zhang, and Z. Lu, "Totem-pole boost bridgeless PFC rectifier with simple zero-current detection and full-range ZVS operating at the boundary of DCM/CCM," *IEEE Trans. Power Electron.*, vol. 26, no. 2, pp. 427–435, Feb. 2011.

[12] W. Y. Choi and J. S. Yoo, "A bridgeless single-stage half-bridge AC/DC converter," *IEEE Trans. Power Electron.*, vol. 26, no. 12, pp. 3884–3895, Dec. 2011.

[13] S. W. Lee and H. L. Do, "Single-stage bridgeless AC–DC PFC converter using a lossless passive snubber and valley switching," *IEEE Trans. Ind. Electron.*, vol. 63, no. 10, pp. 6055–6063, Oct. 2016.

[14] M. Alam, W. Eberle, D. S. Gautam, C. Botting, N. Dohmeier, and F. Musavi, "A hybrid resonant pulse-width modulation bridgeless AC–DC power factor correction converter," *IEEE Trans. Ind. Appl.*, vol. 53, no. 2, pp. 1406–1415, Feb. 2017.

[15] A. Malschitzky, F. Albuquerque, E. Agostini, and C. B. Nascimento, "Single-stage integrated bridgeless-boost nonresonant half-bridge converter for LED driver applications," *IEEE Trans. Ind. Electron.*, vol. 65, no. 5, pp. 3866–3878, May 2018.

[16] H. Ma, Y. Li, J. S. Lai, C. Zheng, and J. Xu, "An improved bridgeless SEPIC converter without circulating losses and input voltage sensing," *IEEE Trans. Emerg. Sel. Topics Power Electron.*, vol. 6, no. 3, pp. 1447–1455, Sep. 2018.

[17] J. W. Shin, S. J. Choi, and B. H. Cho, "High-efficiency bridgeless flyback rectifier with bidirectional switch and dual output windings," *IEEE Trans. Power Electron.*, vol. 29, no. 9, pp. 4752–4762, Sep. 2014.

[18] E. H. Kim and B. H. Kwon, "Zero-voltage- and zero-current-switching full-bridge converter with secondary resonance," *IEEE Trans. Ind. Electron.*, vol. 57, no. 3, pp. 1017–1025, Mar. 2010.

[19] S. Kim, B. Kim, B. H. Kwon, and M. Kim, "An active voltage-doubler rectifier based hybrid resonant DC/DC converter for wide-input-range thermo-electric power generation," *IEEE Trans. Power Electron.*, vol. 33, no. 11, pp. 9470–9481, Nov. 2018.

[20] H. Kim, J. S. Lee, J. S. Lai, and M. Kim, "Iterative learning controller with multiple phase-lead compensation for dual-mode flyback inverter," *IEEE Trans. Power Electron.*, vol. 32, no. 8, pp. 6468–6480, Aug. 2017.

[21] B. Han, J. S. Lai, and M. Kim, "Dynamic modeling and controller design of dual-mode Cuk inverter in grid-connected PV/TE applications," *IEEE Trans. Power Electron.*, vol. 33, no. 10, pp. 8887–8904, Oct. 2018.

[22] Y. Cho and J. S. Lai, "Digital plug-in repetitive controller for single-phase bridgeless PFC converters," *IEEE Trans. Power Electron.*, vol. 28, no. 1, pp. 165–175, Jan. 2013.

[23] C. Wang, X. Li, L. Guo, and Y. W. Li, "A nonlinear-disturbance-observer-based DC-bus voltage control for a hybrid AC/DC microgrid," *IEEE Trans. Power Electron.*, vol. 29, no. 11, pp. 6162–6177, Nov. 2014.

[24] M. Pahlevani and P. Jain, "A fast DC-bus voltage controller for bidirectional single-phase AC/DC converters," *IEEE Trans. Power Electron.*, vol. 30, no. 8, pp. 4536–4547, Aug. 2015.

[25] J. F. Chen, R. Y. Chen, and T. J. Liang, "Study and implementation of a single-stage current-fed boost PFC converter with ZCS for high voltage applications," *IEEE Trans. Power Electron.*, vol. 23, no. 1, pp. 379–386, Jan. 2008.

Sooa Kim (S'15) was born in Seoul, Korea, in 1991. He received the B.S. degree in electrical engineering, in 2013, from the Pohang University of Science and Technology, Pohang, Korea, where he is currently working toward the Ph.D. degree in creative IT engineering.

His research interests include highly efficient power conversion circuits, renewable energy systems, and distributed power generations.

Bong-Hwan Kwon (M'91) was born in Pohang, Korea, in 1958. He received the B.S. degree in electrical engineering from Kyungpook National University, Daegu, Korea, in 1982, and the M.S. and Ph.D. degrees in electrical engineering from the Korea Advanced Institute of Science and Technology, Seoul, Korea, in 1984 and 1987, respectively.

Since 1987, he has been with the Department of Electronic and Electrical Engineering, Pohang University of Science and Technology, Pohang, Korea, where he is currently a Professor. His research interests include converters for renewable energy, high-frequency converters, and switch-mode power supplies.

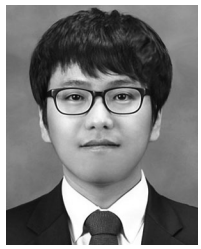

Minsung Kim (M'14) was born in Ulsan, Korea, in 1986. He received the B.S. and Ph.D. degrees in electrical engineering from the Pohang University of Science and Technology (POSTECH), Pohang, Korea, in 2008 and 2013, respectively.

Since 2013, he has been with the Department of Creative IT Engineering and Future IT Research Laboratory, POSTECH, Pohang, South Korea, where he was a Research Assistant Professor. In 2016, he was a Research Scholar with the Future Energy Electronics Center, Virginia Tech, Blacksburg, VA, USA. In 2017, he served as an Academic Visitor with Control and Power System Group, Imperial College London, London, U.K. Since 2018, he has been with the Division of Electronics and Electrical Engineering, Dongguk University, Seoul, Korea, where he is currently an Assistant Professor. His current research interests include highly efficient power conversion circuit design, intelligent controller design for industrial electronics, and renewable energy and energy storage systems.